Monthly Notices
of the
ROYAL ASTRONOMICAL SOCIETY

MNRAS **461,** 2688–2701 (2016)
Advance Access publication 2016 June 8

doi:10.1093/mnras/stw1382

Swift J174540.7−290015: a new accreting binary in the Galactic Centre

G. Ponti,[1]★ C. Jin,[1] B. De Marco,[1] N. Rea,[2,3] A. Rau,[1] F. Haberl,[1] F. Coti Zelati,[2,4,5] E. Bozzo,[6] C. Ferrigno,[6] G. C. Bower[7] and P. Demorest[8]

[1]*Max-Planck-Institut für extraterrestrische Physik, Giessenbachstrasse, D-85748, Garching, Germany*
[2]*Anton Pannekoek Institute for Astronomy, University of Amsterdam, Postbus 94249, NL-1090 GE Amsterdam, the Netherlands*
[3]*Institute of Space Sciences (CSIC-IEEC), Campus UAB, Carrer Can Magrans s/n, E-08193 Barcelona, Spain*
[4]*Universita dellÕInsubria, via Valleggio 11, I-22100 Como, Italy*
[5]*INAF* D *Osservatorio Astronomico di Brera, Via Bianchi 46, I-23807 Merate (LC), Italy*
[6]*Department of Astronomy, University of Geneva, Chemin dÕEcogia 16, CH-1290 Versoix, Switzerland*
[7]*Academica Sinica Institute of Astronomy and Astrophysics, 645 N. A'ohoku Place, Hilo, HI 96720, USA*
[8]*National Radio Astronomy Observatory, PO Box O, Socorro, NM 87801, USA*

Accepted 2016 June 3. Received 2016 June 3; in original form 2016 April 1

ABSTRACT

We report on the identification of the new Galactic Centre (GC) transient Swift J174540.7−290015 as a likely low-mass X-ray binary located at only 16 arcsec from Sgr A⋆. This transient was detected on 2016 February 6, during the *Swift* GC monitoring, and it showed long-term spectral variations compatible with a hard- to soft-state transition. We observed the field with *XMM–Newton* on February 26 for 35 ks, detecting the source in the soft state, characterized by a low level of variability and a soft X-ray thermal spectrum with a high energy tail (detected by *INTEGRAL* up to ∼50 keV), typical of either accreting neutron stars or black holes. We observed: (i) a high column density of neutral absorbing material, suggesting that Swift J174540.7−290015 is located near or beyond the GC and; (ii) a sub-Solar iron abundance, therefore we argue that iron is depleted into dust grains. The lack of detection of Fe K absorption lines, eclipses or dipping suggests that the accretion disc is observed at a low inclination angle. Radio (Very Large Array) observations did not detect any radio counterpart to Swift J174540.7−290015. No evidence for X-ray or radio periodicity is found. The location of the transient was observed also in the near-infrared (near-IR) with gamma-ray burst optical near-IR detector at MPG/European Southern Observatory La Silla 2.2 m telescope and VLT/*NaCo* pre- and post-outburst. Within the *Chandra* error region, we find multiple objects that display no significant variations.

Key words: methods: observational – techniques: spectroscopic – X-rays: binaries.

1 INTRODUCTION

Sgr A⋆(Genzel et al. 2010), the supermassive black hole (BH) at the Galactic Centre (GC), generates a deep gravitational potential that is expected to bind tens of thousands of stellar remnants, such as neutron stars (NS) or BH that have settled dynamically into the central parsec of the Milky Way (Morris 1993; Lee 1995; Miralda-Escudé & Gould 2000; Muno et al. 2005). Deep radio surveys were so far unsuccessful in detecting either ordinary or millisecond pulsars, leading to the 'missing pulsar problem' (Wharton et al. 2012; Dexter & O'Leary 2014). Surprisingly, a few years ago, the magnetar SGR J1745−2900 was discovered via its outburst activity (Eatough et al. 2013; Mori et al. 2013; Rea et al. 2013; Kaspi et al. 2014; Coti Zelati et al. 2015), representing the first radio and X-ray pulsar discovered in the Galactic Centre region (at less than a few parsecs from Sgr A⋆). Many millisecond radio pulsars are expected in the region, but currently not a single one has been detected. Due to the three body interaction between this concentration of degenerate stars and multiple stellar systems, a large population of X-ray binaries is also expected. The monitoring of X-ray transients allows us to study this population (Pfahl & Loeb 2004; Muno et al. 2005; Hopman 2009; Faucher-Giguère & Loeb 2011).

The majority of accreting X-ray binaries spend most of their time in a quiescent state (below the detection limit), sporadically interrupted by outbursts during which the X-ray luminosity rises by many orders of magnitudes (Fender & Belloni 2012). Pioneering works on monitoring of GC X-ray sources have been performed with *Chandra* and *Swift* (Muno et al. 2005; Wijnands et al. 2006; Campana 2009; Degenaar et al. 2012, 2015).

Swift J174540.7−290015 was discovered by the *Swift* satellite on 2016 February 6 (Reynolds et al. 2016), during the first X-ray observation after the GC exited the Solar constraint window. The *Swift* X-ray telescope (XRT) data showed a bright

⋆ E-mail: ponti@iasfbo.inaf.it

($F \sim 2 \times 10^{-10}$ erg cm^{-2} s^{-1}, in the 2–10 keV range) transient located at less than 16 arcsec from Sgr A* (Reynolds et al. 2016). Swift J174540.7−290015 was detected also in the 20–80 keV energy range (Esposito et al. 2016), while observations with the Karl G. Jansky Very Large Array (VLA) and Giant Metrewave Radio Telescope did not detect the radio counterpart (however the limits still leave open the possibility of a hard-state accreting BH or NS) or any pulsation (Bower et al. 2016; Maan et al. 2016). Within a week from this discovery, *Chandra* observed the field and refined the transient position to: $\mathrm{RA_{J2000}}$ =17:45:40.66 ± 0.34, $\mathrm{Dec_{J2000}}$ =−29:00:15.61 ± 0.33, where no previous X-ray sources were ever detected (Baganoff et al. 2016). Therefore, Swift J174540.7−290015 is a new transient source.

In this paper, we report the identification of the source as a low-inclination X-ray binary hosting an NS or a BH, most probably with a low-mass companion. We discuss the temporal and spectral characteristics of the transient using the long-term daily X-ray monitoring of the field performed by the *Swift* satellite, the high energy long-term monitoring provided by the *INTEGRAL* satellite, a 35 ks *XMM–Newton* observation obtained in Director's Discretionary Time (to study the dust scattering halo) performed about 20 d after the onset of the outburst as well as VLA observations. Finally, we report on the search for the near-infrared (near-IR) counterpart within VLT/*NaCo* and gamma-ray burst optical near-IR detector (GROND) data.

2 X-RAY OBSERVATIONS AND DATA REDUCTION

2.1 *XMM–Newton*

XMM–Newton (Jansen et al. 2001) observed Swift J174540.7−290015 on February 26 for 35 ks. We processed this data set starting from the observation data files. The data have been treated using the latest version (15.0.0) of the *XMM–Newton* Science Analysis System (SAS) with the most recent (2016 March 13) calibrations. We used all European Photon Imaging Camara (EPIC) (Strüder et al. 2001; Turner et al. 2001) cameras equipped with the medium filter. The arrival times of the events were corrected to the Solar system barycentre, applying the BARYCEN task of SAS. We screened the periods of enhanced particle-induced activity by inspecting the EPIC-pn 10–15 keV light curves, binned with 5 s resolution, extracted from a circular region, with 5 arcmin radius, close to the border of the field of view. We then filter out all the periods with more than 0.85 cts s^{-1}.

Since the main focus of the observation was the study of the full extension of the dust scattering halo around the source, the EPIC-pn camera was in Full Frame mode. Having a frame time of 73.4 ms, the inner core of the point spread function (PSF) shows pile-up. On the other hand, both EPIC-MOS1 and MOS2 were in timing mode, with a frame time of 1.75 ms. This assures that no pile-up is present in these data sets. A bad column is falling in the centre of the extraction region in the EPIC-MOS1 camera, inducing lower statistics. Therefore these data have been used for consistency checks only. To reduce pile-up, the source photons in the EPIC-pn camera were extracted from an annular region. The outer radius of the annulus was limited to 40 arcsec, to avoid contribution from the low mass X-ray binary (LMXB) AX J1745.6−2901 (Ponti et al. 2015b) and the inner radius has been fixed to 15 arcsec. By comparing this spectrum from the wings of the PSF with the pile-up free EPIC-MOS2 spectrum, we verified that it is not affected by pile-up. We note that the magnetar SGR J1745−2900 (Rea et al. 2013) is located inside the source extraction region. However, the magnetar is currently observed at a 2–10 keV flux of $F_{2\text{-}10} = 3.8 \times 10^{-13}$ erg s^{-1} cm^{-2}, about three orders of magnitude lower than the instantaneous 2–10 keV flux of Swift J174540.7−290015 ($F_{2\text{-}10} = 2.9 \times 10^{-10}$ erg s^{-1} cm^{-2}). Therefore, SGR J1745−2900 gives a negligible contribution to the light curves and spectra of Swift J174540.7−290015.

A strong contribution from the emission of the supernova remnant Sgr A East (Maeda et al. 2002; Ponti et al. 2015c) is expected within the EPIC-pn extraction region of Swift J174540.7−290015, therefore, we extracted the background plus diffuse emission from a long archival observation (ObsID 0505670101) during which AX J1745.6−2901 had flux and spectral properties similar to the ones during this observation (being in the soft state and at similar flux), the magnetar SGR J1745−2900 was in quiescence and Sgr A* did not show any flare (Ponti et al. 2015d). In the EPIC-MOS2 camera, the source photons were extracted between RAWX 285 and 330. The larger extraction region, imposed by the timing mode, implies a larger contribution from AX J1745.6−2901 and diffuse emission, compared to the EPIC-pn spectrum. We converted the source extraction region (from RAWX coordinates into sky coordinates through the SAS task ECOORDCONV) and we extracted the background plus diffuse emission from the EPIC-MOS2 camera, during the same long observation (OBSID 0505670101) with Swift J174540.7−290015 in quiescence. Because of the higher contamination by AX J1745.6−2901, we use the EPIC-MOS spectra for comparison only. We note that the same best-fitting parameters (with all values consistent with the ones obtained by fitting the EPIC-pn spectrum; Section 4) were obtained by fitting the EPIC-MOS spectra.

The combination of high column density of absorbing material ($N_{\rm H} = 18.7 \times 10^{22}$ cm^{-2}) and the intense diffuse emission in the direction towards the GC, prevents us from obtaining a good characterization of the source emission below ∼2 keV (e.g. the low energy absorption edges). For this reason in this work, we do not consider the data from the Reflection Grating Spectrometer instruments.

Spectral fitting was performed using XSPEC version 12.8.2. The spectra were grouped so that each bin contains at least 30 counts.

2.2 Swift

The *Swift* XRT has been monitoring the central ∼15 arcmin of the Galaxy daily since year 2012 (Degenaar et al. 2015). We downloaded all the *Swift* PC mode data sets between 2016 February 5 and 2016 March 10 from the HEASARC data archive. This comprises 31 PC mode XRT observations. To characterize the contribution from the background plus complex diffuse emission within the extraction region of Swift J174540.7−290015 (that contains a contribution from SGR J1745−2900 and AX J1745.6−2901), we used the *Swift* data before the outburst of Swift J174540.7−290015. Since there was no *Swift* observation of this region between 2015 November 3 and 2016 February 5, we retrieved 15 *Swift* observations between 2015 October 15 and 2015 November 2 in XRT PC mode when the source was quiescent. These 15 observations are used to measure the background plus diffuse emission underneath Swift J174540.7−290015.

We applied the standard data reduction following the threads described on the *Swift* website. Because of the high absorption column density towards the source, we considered only data in the 2–10 keV band. Images and spectra were produced using the XSELECT (v2.4c) package. Since Swift J174540.7−290015 is very

bright, significant pile-up is affecting all the PC mode observations. We followed the standard XRT pile-up thread to determine the pile-up level. We extracted the products from an annulus with inner radius of 15 arcsec, to ensure that spectra, fluxes and light curves are not affected by pile-up. A 40 arcsec outer radius is used to include most source flux and less contamination from AX J1745.6−2901. We manually adjusted the astrometry of all data sets by visually inspecting the images of all the observations. This has been obtained by adjusting the relative position between Swift J174540.7−290015 and AX J1745.6−2901. This allows us to correct the astrometry shifts, which would otherwise affect the PSF correction and the correct determination of the source flux. By comparing the light curve with that derived without PSF correction, we ensured that the uncertainties in the PSF correction are not the cause of the observed source variability. We also note that the background flux underneath Swift J174540.7−290015 is only 3 per cent of the source flux in the 2–10 keV band, so it does not significantly contaminate the light curve of Swift J174540.7−290015, either.

In addition to the PC mode data, there are also 12 *Swift* XRT Windowed Timing (WT) mode observations of Swift J174540.7−290015. Compared to the PC mode, the WT mode provides higher time resolution and more counts, but the one-dimensional image in the WT mode makes it difficult to determine the background underneath the source region from previous observations as we did in the PC mode. However, since the background flux is only 3 per cent of the source flux, we use anyway the WT mode observations as an independent check of the PC mode results.

Swift J174540.7−290015 is not piled up in the WT mode, so we defined a circular source region of 20 arcsec radius, centred on the pixel which is the perpendicular projection of the source position on the one-dimensional WT mode image (again we consider only data in the 2–10 keV band). The choice of 20 arcsec radius was a compromise between including more source flux and less contamination from AX J1745.6−2901. For 11 WT mode observations, there were also PC mode observations on the same day, for which we could compare the spectra between the two modes. For nine observations, both the spectral shape and normalization were consistent between the two modes, except that WT mode provided more counts and thus higher signal-to-noise ratio (S/N). The remaining two WT mode spectra (ObsID: 00035063134, 00035063136) have the same spectral shape as in the PC mode but with different normalization. We found that this is caused by the bad pixels within the source extraction region in these two WT mode observations, which affected the source flux and PSF correction, but did not affect the spectral shape. We excluded these two observations from further analysis. Since the source spectra from WT mode observations were consistent with the PC mode, and the background underneath Swift J174540.7−290015 was much weaker than the source itself, we decided to apply the same background flux and spectra for the WT mode data as for the PC mode, and this should not affect our results.

The exposure maps and ancillary files for the spectra were computed with the XRTEXPOMAP and XRTMKARF tools provided in the HEASOFT (6.18) software.

2.3 *INTEGRAL*

The outburst of the source was observed by *INTEGRAL* starting from 2016 February 11, i.e. during satellite revolution 1643. At the time of writing, only consolidated *INTEGRAL* data up to revolution 1652 were made available and thus we were able to observe the evolution of the source hard X-ray emission until 2016 March 6. As the source is located right into the GC, which is a complex and crowded region, we also made use of the last data collected towards this region before the outburst of Swift J174540.7−290015. These included data during revolutions 1597, 1603 and 1604, covering the period from 2015 October 11 to 19.

INTEGRAL observations are divided into 'science windows' (SCWs), i.e. pointings with typical durations of ∼2–3 ks. We considered only SCWs, where the source was within a maximum off-axis angle of 12 deg from the satellite aim point, in order to reduce the uncertainties on the energy calibrations. All data were analysed by using version 10.2 of the Off-line Scientific Analysis software (OSA) distributed by the INTEGRAL Science Data Centre (ISDC) (Courvoisier et al. 2003). We first extracted the Imager on Board the INTEGRAL Satellite (IBIS)/CdTe array (ISGRI) (Ubertini et al. 2003; Lebrun et al. 2003) mosaics in the 20–100 keV energy band and the Joint European Monitor for X-rays (JEM-X) (Lund et al. 2003) mosaics in the 3–10 keV energy band by summing up all data in revolutions 1597 to 1604. No source was detected at a position consistent with Swift J174540.7−290015 in the 20–100 keV energy band and we estimated a 3σ upper limit on the corresponding energy range of 3 mCrab (corresponding[1] to roughly 5.4×10^{-11} erg cm^{-2} s^{-1}). From the JEM-X mosaic, we noticed that the well-known transient LMXB AX J1745.6−2901 (Ponti et al. 2015b) was detected at a position consistent with that of Swift J174540.7−290015. The limited spatial resolution of the JEM-X instrument does not allow us to disentangle the emission of AX J1745.6−2901 from the one of Swift J174540.7−290015. Therefore, we decided to extract a JEM-X spectrum of AX J1745.6−2901 from observation taken before the outburst of Swift J174540.7−290015. We then used this file as a background for the spectrum of Swift J174540.7−290015 that we obtained from the later observations (we checked in the *Swift* data that AX J1745.6−2901 did not go through major flux and/or state changes during the considered period). The JEM-X spectrum of AX J1745.6−2901 could be well fit ($\chi^2_{\rm red}$/dof = 0.5/5) with a power-law model of photon index $\Gamma = 2.2 \pm 0.5$ ($F_{3-10\,\rm keV} \sim 3.5\times10^{-10}$ erg cm^{-2} s^{-1}).[2]

For all *INTEGRAL* revolutions from 1643 to 1652, we built the IBIS/ISGRI and JEM-X mosaics and extracted the source spectra in 13 energy bins for ISGRI and 8 energy bins for JEM-X (we used data from both the JEM-X1 and JEM-X2 units). The JEM-X spectrum obtained during revolution 1643 revealed a 3–20 keV flux of $F_{3-20\,\rm keV} = 1.0\times10^{-9}$ erg cm^{-2} s^{-1}, therefore, AX J1745.6−2901 contaminated the emission from Swift J174540.7−290015 by no more than 30 per cent. As AX J1745.6−2901 was not detected in the previous IBIS/ISGRI mosaic, the recorded 20–100 keV X-ray flux of 7.4×10^{-10} erg cm^{-2} s^{-1} is to be completely attributed to Swift J174540.7−290015. This object remained bright in all *INTEGRAL* data we used, and was detected at high significance in the IBIS/ISGRI and JEM-X mosaics of all revolutions.

2.4 Karl G. Jansky Very Large Array (VLA)

VLA observations of Swift J174540.7−290015 were carried out on two epochs, 2016 February 25 and 2016 March 25. As we will

[1] The conversion between the upper limit on the source count rate and flux has been done by using the observations of the Crab in revolution 1597, as described in Bozzo et al. (2016).

[2] Note that in order to avoid contamination issues, both the JEM-X and ISGRI spectra used in this work were extracted from the instrument mosaics with the MOSAIC_SPEC tool rather than running the OSA software down to the SPE level (see discussion in Bozzo et al. 2016).

Table 1. VLA image summary.

Epoch	UT	Centre frequency (GHz)	Beam	rms (mJy)
2016 February 25	16:28–17:09 UT	6.0	$7.8'' \times 2.3''$, 22°	53
–	–	15.0	$4.3'' \times 0.9''$, 29°	6
2016 March 25	13:45–14:45 UT	6.0	$6.3'' \times 2.2''$, 18°	53
–	–	15.0	$3.5'' \times 0.9''$, 22°	14

discuss later (see Section 5.1), Swift J174540.7−290015 was in the soft state during at least the first of these VLA observations. In each epoch, data were obtained in two frequency bands, C and Ku, with centre frequencies of 6.0 and 15.0 GHz, respectively. The VLA correlator was simultaneously configured for imaging and a phased array beam centred on Swift J174540.7−290015. The VLA was in its C configuration for both observations with a maximum baseline length of 3 km.

Imaging data were obtained over frequency ranges of 3.976–8.072 GHz and 12.952–17.048 GHz, respectively. The correlator was configured to produce cross-correlations that were split into 64 frequency windows each with 128 channels in dual circular polarization. These imaging data were reduced using the CASA VLA pipeline. The radio galaxy 3C 286 was used to set the flux calibration and the compact source J1744−3116 was used as a phase calibration source for Swift J174540.7−290015. Additional steps of self-calibration with Sgr A* as the reference were performed using only visibilities with baselines longer than 50 $k\lambda$ and 20 $k\lambda$ in Ku and C bands, respectively. Images of the Swift J174540.7−290015 field using only these long baseline visibilities were produced. These long baselines filtered out much of the substantial emission associated with the northern arm of Sgr A West. Details of the epochs and images are summarized in Table 1. No radio source was identified at the location of *Swift* in either epoch at either frequency.

We also recorded high time resolution data from a phased array beam at the position of Swift J174540.7−290015. In both frequency bands, these data were taken with 4.096 GHz total bandwidth divided into 1024 frequency channels at 250 μs time resolution. We searched for dispersed, periodic signals over dispersion measures ranging from 0 to 10 000 pc cm^{-4} and pulse frequency drift (source acceleration) up to 5×10^{-5} Hz s^{-1}. At both frequencies, pulses from the bright, nearby 3.76 s magnetar PSR J1745−2900 were detected with high S/N, but no other significant periodicities were found. Assuming 10 per cent pulse duty cycle, the 10σ flux density limits for the periodicity searches were 30 μJy at *C* band and 45 μJy at *Ku* band.

Throughout the paper, we assume a distance to the source equal to 8 kpc (Genzel et al. 2010; Gillessen et al. 2013). Error-bars are quoted at the 90 per cent confidence level for a single parameter of interest. We also assume that the accretion disc is observed face on. This is in agreement with the indication (Section 3.1) that the system is observed at low inclination ($i < 60°$; Frank, King & Lasota 1987; Díaz-Trigo et al. 2006; Ponti et al. 2016). Would the inclination be $i = 60°$, the inner disc radii and luminosities would be 1.4 and 2 times larger, respectively.

3 SHORT-TERM VARIABILITY

3.1 The *XMM–Newton* light curve

Fig. 1 shows the PSF-corrected EPIC-pn light curve in the 2–10 keV band with 200 s bins. No variability is observed and the data are well

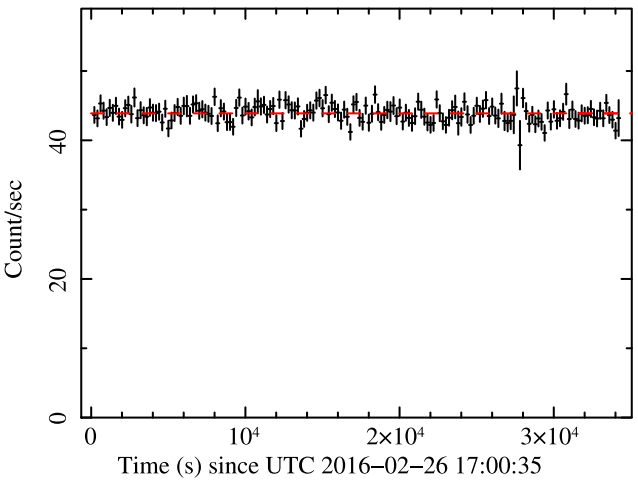

Figure 1. PSF corrected EPIC-pn light curve of Swift J174540.7−290015 in the 2–10 keV band. The light curve is extracted from an annular region with inner and outer radii of 15 arcsec and 40 arcsec, respectively, and binned at 200 s. No bursts (not even in 1 s binned light curves) or dips are observed. The red dashed line shows the best fit with a constant (that results in 43.9 cts s^{-1} and $\chi^2 = 161.7$ for 170 dof).

fit with a constant that is shown by the red dashed line ($\chi^2 = 161.7$ for 170 degrees of freedom; dof). No bursts or dipping events are observed during the *XMM–Newton* observation (White & Mason 1985; Frank et al. 1987; Díaz-Trigo et al. 2006). To refine our capability to detect bursts and dips, we investigated a variety of energy bands and time bins. No bursts are detected in light curves with time bins, as short as sub-second. We also investigated soft energy bands, where the effect of dipping is stronger (Díaz-Trigo et al. 2006; Ponti et al. 2016), and their hardness ratio, but no dipping events were found.

3.2 Timing analysis: broad-band noise

We extracted MOS and pn light curves in the energy bands 2–10 keV, 2–6 keV and 6–10 keV, with a time resolution of 3.5 ms and 200 ms, respectively. The power spectral density function (PSD) was computed in each energy band and for each instrument separately. The Poisson noise level was estimated from the mean power at frequencies >50 Hz, where counting noise variability dominates. The relatively long frame time of the EPIC pn instrument in full frame observing mode prevents us from sampling these frequencies. Therefore, the Poisson noise level cannot be accurately estimated, thus we did not consider the EPIC-pn PSD further.

Fig. 3 shows the PSD of the MOS data in the 2–10 keV band. For comparison, we also plot the PSD of the BH X-ray binary GX 339-4 in a high-luminosity hard state (De Marco et al. 2015). Swift J174540.7−290015 displays significantly less power than

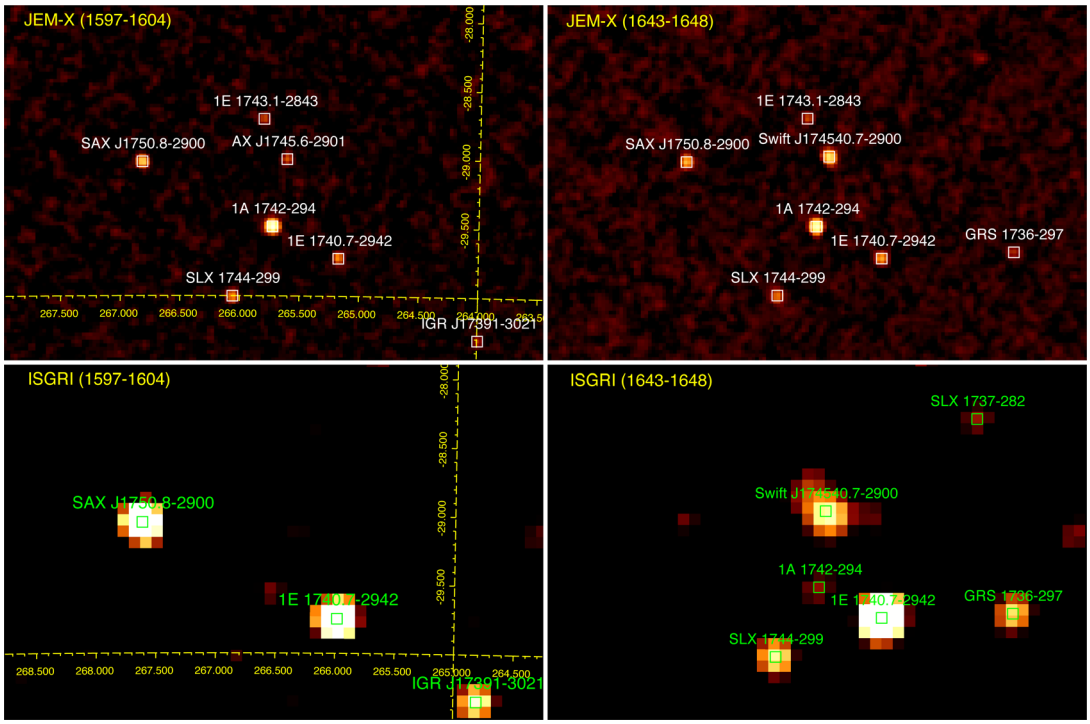

Figure 2. Mosaiked JEM-X (3–10 keV) and IBIS/ISGRI (20–40 keV) images around the position of Swift J174540.7−290015 obtained from the revolutions 1597–1604 performed before the source outburst (top and bottom left) and the revolutions 1643–1648 performed during the first part of the source outburst (top and bottom right). As it can be seen, Swift J174540.7−290015 is only detected from revolution 1643 onward in IBIS/ISGRI, while in JEM-X AX J1745.6−2901 is detected in the earlier revolutions at a position consistent with *Swift* (albeit at a much lower luminosity; see the text for details).

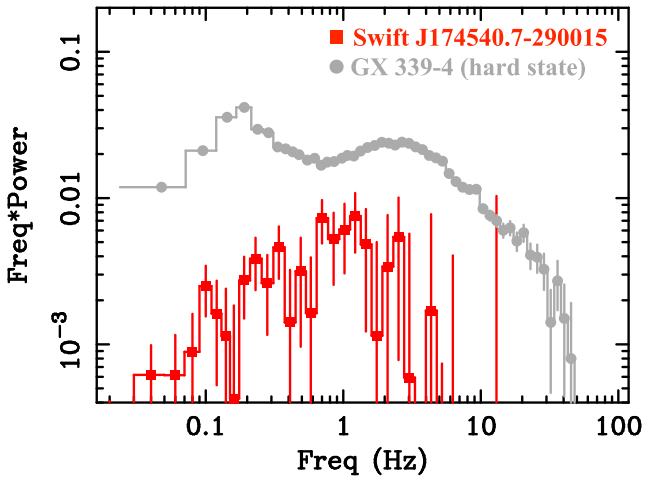

Figure 3. The PSD [in units of (rms/mean)^2] of Swift J174540.7−290015 (red squares), computed from MOS2 data in the 2–10 keV energy band. The 2–10 keV PSD of GX 339-4 in a high-luminosity hard state (De Marco et al. 2015) is reported for comparison (grey dots).

observed in a typical hard state of a BHXRB. Indeed, the 2–10 keV fractional root-mean-square (rms) variability amplitude (e.g. Nandra et al. 1997; Vaughan et al. 2003; Ponti et al. 2004) in the 0.1–64 Hz frequency interval is estimated to be 0.07 ± 0.02. This value is consistent with what is typically observed in either a BH or NS XRB in a soft/soft-intermediate state (Muñoz-Darias, Motta & Belloni 2011; Muñoz-Darias et al. 2014).

3.3 Timing analysis: search for periodic signals

We searched for periodic signals using the *XMM–Newton* pn and MOSs data, as well as *Swift* WT-mode data (being sensible to signals between the Nyquist frequency, and the frequency resolution of each data set; van der Klis 1988). We used a modified version of the XRONOS analysis software to search for periodicities following the prescriptions described in Vaughan et al. (1994), and we did not find any periodic or quasi-periodic signal in any of the reported X-ray observations (we had accounted for the number of bins searched, and the different dof of the noise power distribution in the non-detection level). We have searched all data set performing Fast Fourier Transforms over the total length of the observations, but also over small intervals of 0.5, 1, 3 and 5 ks in order to search for signals that might have been possibly smeared by Doppler shifts due to hour-long orbital periods. Unfortunately, the data set with by far the largest number of counts, the EPIC-pn, had a timing resolution of ∼73 ms, making our searches rather insensitive to fast spinning pulsars (i.e. with spin periods of ∼ twice this value).

We computed the 3σ upper limits on the sinusoid semi-amplitude pulsed fraction (PF) according to Vaughan et al. (1994) and Israel & Stella (1996). The deepest limits at frequencies <6 Hz were derived from the EPIC-pn data, having the larger number of collected photons. Note that given the nature of this source, if a very short orbital period causes Doppler smearing of the putative signal (i.e. if the signal is not strong enough to be detected in our small ∼1 ks chunks that might be free of Doppler smearing), these PF limits are not constraining. To have a handle on the PF limits on faster periodicities (anyway smaller than 300 Hz), we used the MOSs data (taken in timing mode: 1.75 ms timing resolution) as well as the *Swift* WT data (1.7 ms timing resolution), although having to cope with a much reduced number of counts, and again using the

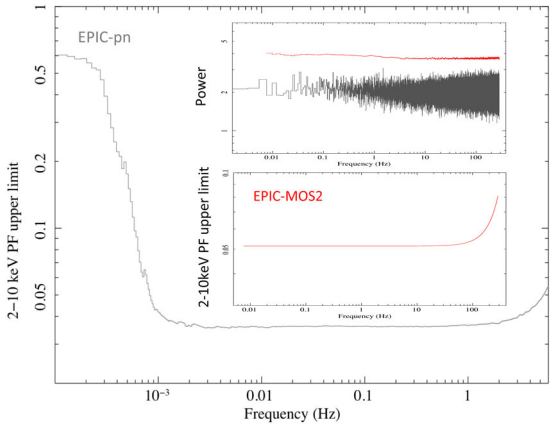

Figure 4. (Main panel) Pulsed fraction 3σ upper limits as derived for the 2–10 keV EPIC-pn. The fractional PF is in units of 100 per cent. (Upper inset) MOS2 power density spectra. (Lower inset) Fractional pulsed fraction 3σ upper limits as derived for the 2–10keV MOS2.

full length of the observation and searching in small consecutive time intervals. We show the resulting 3σ upper limit on the PF of a periodic signal (if not Doppler smeared in the presence of a short orbital period) for both pn and MOS2 data in Fig. 4.

4 SPECTRAL ANALYSIS OF THE DEEP *XMM–Newton* OBSERVATION

4.1 Characterization of the mean spectrum

We fit the EPIC-pn spectrum by always including an absorption component from neutral matter plus the contribution from the dust scattering halo. The neutral absorption is fitted with the model TBNEW (see Wilms, Allen & McCray 2000) with cross-sections of Verner et al. (1996) and abundances of Wilms et al. (2000). The dust scattering halo is fitted with the model DUST (Predehl & Schmitt 1995). We assume that the dust scattering optical depth at 1 keV is tied to the X-ray absorbing column density by the relation: $\tau = 0.324 \times (N_{\rm H}/10^{22}\,{\rm cm}^{-2}$; as in Nowak et al. 2012). However, we note that a more proper modelling of the dust scattering effect on the observed spectrum requires better knowledge about the location and properties of the dust along the line of sight (Smith, Valencic & Corrales 2016), as well as a better constrained location of Swift J174540.7−290015, which would then require detailed analysis of the extended emission from the dust scattering halo. This is already beyond the scope of this paper, but will be included in our further study.

We first fit the spectrum with a series of single component models. We start with an absorbed power-law model (DUST*TBNEW*POWERLAW in XSPEC). Large residuals remain at high energy ($\chi^2 = 1530.9$ for 1189 dof; see Table 2). Moreover, the best-fitting power-law spectral index is unrealistically steep ($\Gamma = 5.76 \pm 0.04$), clearly indicating the thermal nature of this emission. Therefore, we fit the spectrum with either an absorbed blackbody (DUST*TBNEW*BBODY) or an absorbed multitemperature disc blackbody component (DUST*TBNEW*DISKBB). None of these two models provides an acceptable fit, all leaving significant residuals at high energies (see Table 2).

The large residuals at high energy clearly indicate the presence of a second emission component. Therefore, we add to the thermal emission model the contribution provided by a thermal Comptonization component (reproduced by the NTHCOMP model; Zdziarski, Johnson & Magdziarz 1996; Życki, Done & Smith 1999). Being the high energy cutoff outside of the *XMM–Newton* energy band, we fix the electron temperature to a high value of $E = 50$ keV (consistent results are obtained by fixing the electron temperature to e.g. 20 or 100 keV). The fit with an absorbed blackbody plus thermal Comptonization model provides a satisfactory description of the data (see Table 3). The best-fitting blackbody temperature is $kT_{\rm BB} = 0.54 \pm 0.01$ keV produced from a surface area with radius $R_{\rm BB} = 35 \pm 11$ km. The fit with an absorbed multitemperature disc blackbody plus Comptonization emission, provides a temperature of $kT = 0.66 \pm 0.02$ keV and a very reasonable inner disc radius of $r_{\rm in} \sim 27 \pm 10$ km (or $\sim$6.5 $r_{\rm S}$, with $r_{\rm S} = 2GM/c^2$, where G is the gravitational constant, M is the mass of the primary, assumed to be $M = 1.4\,{\rm M}_{\odot}$ and c is the speed of light); however, the fit is slightly worse (see Table 3). Nevertheless, in both these cases, we observe a rather steep spectral index of the Comptonization component, with values of $\Gamma \sim 3.5$–3.8. Therefore, we substituted the Comptonization component with a second thermal component. On a statistical ground, we obtained an improved solution with the sum of an absorbed blackbody (with $kT_{\rm BB} = 0.56 \pm 0.01$ keV) plus a multitemperature disc blackbody emission ($kT_{\rm DBB} = 1.86 \pm 0.14$ keV). However, we note that the best-fitting inner radius of the disc blackbody component is $r_{\rm in} = 0.76 \pm 0.5$ km, therefore, inside the NS surface (see Table 3). For this reason, we think that this solution is unlikely. We note a second minimum in the χ^2 distribution ($\chi^2 = 1262.7$ for 1187 dof), leading to a solution with $kT_{\rm BB} = 1.58 \pm 0.01$ keV plus a multitemperature disc blackbody emission ($kT_{\rm DBB} = 0.68 \pm 0.01$ keV). The best-fitting inner radius of the disc blackbody component now results to be $r_{\rm in} = 26 \pm 9$ km (corresponding to $\sim 6\ r_{\rm S}$), while the blackbody component is produced from a region with radius of $r \sim 1$ km (Table 3).

In conclusion, the shape of the *XMM–Newton* spectrum is dominated by a thermal component (either blackbody or disc blackbody,

Table 2. Best-fitting parameters of the EPIC-pn and MOS2 spectra with a single component models. Column densities ($N_{\rm H}$) are in units of 10^{22} cm^{-2}, temperatures ($kT_{\rm BB}$ and $kT_{\rm DBB}$) are in units of keV, the power-law normalization ($A_{\rm PL}$) is units of photons keV^{-1} cm^{-2} s^{-1} at 1 keV, the disc blackbody normalization ($A_{\rm DBB}$) is in units of $(R_{\rm in}/km)^2/(D/10\ {\rm kpc})^2$, where $R_{\rm in}$ is the apparent inner disc radius (in km units), D is the distance to the source (in 10 kpc units) and the blackbody normalization ($A_{\rm BB}$) is in units of $L_{39}/(D/10\ {\rm kpc})^2$, where L_{39} is the source luminosity in units of 10^{39} erg^{-1}.

Single component model	
DUST*TBNEW*POWERLAW	
$N_{\rm H}$	25.6 ± 0.2
Γ	5.76 ± 0.04
$A_{\rm PL}$	128 ± 8
χ^2/dof	1530.9/1189
DUST*TBNEW*BBODY	
$N_{\rm H}$	13.7 ± 0.2
$kT_{\rm BB}$	0.693 ± 0.003
$A_{\rm BB}$	0.0152 ± 0.0003
χ^2/dof	2897.9/1189
DUST*TBNEW*DISKBB	
$N_{\rm H}$	15.9 ± 0.1
$kT_{\rm DBB}$	0.832 ± 0.006
$A_{\rm DBB}$	278 ± 14
χ^2/dof	2479.3/1189

Table 3. Best-fitting parameters of the EPIC-pn and MOS2 spectra with two component models. For the definition of the units of the parameters, see Table 2. †These are the parameters associated with the second minimum in the χ^2 distribution.

	Double component model ABS = DUST*TBNEW			
	ABS*(BBODY+NTHCOMP)	ABS*(DISKBB+NTHCOMP)	ABS*(BBODY+DISKBB)	ABS*(DISKBB+BBODY)†
Model	(1)	(2)	(3)	(4)
$N_{\rm H}$	17.0 ± 0.3	18.7 ± 0.3	16.9 ± 0.3	18.5 ± 0.3
$kT_{\rm BB}$	0.54 ± 0.01		0.56 ± 0.01	1.58 ± 0.01
$A_{\rm BB}$	1900 ± 200		1882 ± 190	$1.6\pm^{+0.7}_{-0.5}$
$kT_{\rm DBB}$		0.66 ± 0.02	1.86 ± 0.14	0.68 ± 0.01
$A_{\rm DBB}$		1170^{+180}_{-150}	$0.9^{+0.5}_{-0.3}$	1060 ± 130
Γ	3.8 ± 0.3	3.4 ± 0.4		
A_Γ	$6.7^{+2.6}_{-1.9} \times 10^{-2}$	$4^{+6}_{-3} \times 10^4$		
χ^2/dof	1255.2/1187	1272.8/1187	1246.2/1187	1262.7/1187

with temperature of $kT_{\rm BB} \sim 0.55$, $kT_{\rm DBB} \sim 0.67$ keV) plus an additional component at higher energy that could be reproduced either by a steep Comptonization component (perhaps associated with the corona seen in accreting systems) or a blackbody emission (possibly generated by the hotter parts on the surface of an NS). Any of these possibilities appear viable, based uniquely on the *XMM–Newton* data. In Sections 5.1 and 5.2, we will investigate further the source radiative process and we will break this model degeneracy by studying the *Swift* and *INTEGRAL* long-term spectral evolution.

4.2 Ionized absorption

High-inclination accreting BH and NS are known to display ionized absorption features, whenever they are observed in the soft state (Neilsen & Lee 2009; Ponti et al. 2012, Ponti et al. 2016). No narrow Fe K absorption or emission line is evident in the spectra of Swift J174540.7−290015. Fitting the spectrum with additional narrow Gaussian absorption lines, we compute upper limits on the line equivalent width (EW) as stringent as EW < 10 eV to the presence of Fe XXV and Fe XXVI lines, therefore, excluding the presence of either a disc wind or an ionized atmosphere (Díaz-Trigo et al. 2006; Ponti et al. 2012, 2015a, 2016; Ponti, Muñoz-Darias & Fender 2014 b; Miller et al. 2015). Similar upper limits are valid for narrow emission lines between 6.4 and 7 keV. We also note that the addition of a broad Fe K emission line is not required.

4.3 X-ray properties of the ISM

The observation of this bright state of Swift J174540.7−290015 allows us to investigate the properties of the interstellar medium (ISM) along a line of sight placed at less than ∼16 arcsec from Sgr A* (Baganoff et al. 2016). To perform the investigation of the X-ray properties of the ISM, we reproduced the source emission with the absorbed disc blackbody plus blackbody model (model 4 in Section 4.1 and Table 3). The absorption is fitted with the TBNEW model and the effect of the dust scattering halo was taken into account (see Table 3). We observed that using the PHABS absorption model, we measure a column density of absorbing material ($N_{\rm H} = 18.3 \pm 0.3 \times 10^{22}$ cm^{-2}) consistent with the values observed using TBNEW or TBABS. On the other hand, a significantly lower value is observed if either the WABS model ($N_{\rm H} = 12.6 \pm 0.2 \times 10^{22}$ cm^{-2}) or the Anders & Grevesse (1989) Solar abundances ($N_{\rm H} = 12.1 \pm 0.2 \times 10^{22}$ cm^{-2}) are used.

Starting again from the best-fitting baseline model, we explored the possibility to constrain the abundances of the various elements. We did so by leaving the abundance of any metal producing edges in the 2–10 keV band free to vary (see Fig. 5). We observe that the abundances of Si, Cl, Cr, Ca and Co are unconstrained, therefore we left their abundances fixed at the Solar value. On the other hand, iron ($A_{\rm Fe} = 0.5 \pm 0.4$ Solar) and Argon ($A_{\rm Ar} < 0.9$ Solar) are under abundant, compared to Solar, while Sulphur ($A_{\rm S} = 1.25^{+0.19}_{-0.14}$ Solar) appears to be slightly overabundant. We note that a larger column density of absorbing material is required ($N_{\rm H} = 20.1 \pm 1.2 \times 10^{22}$ cm^{-2}), once the iron abundance is left free to vary.

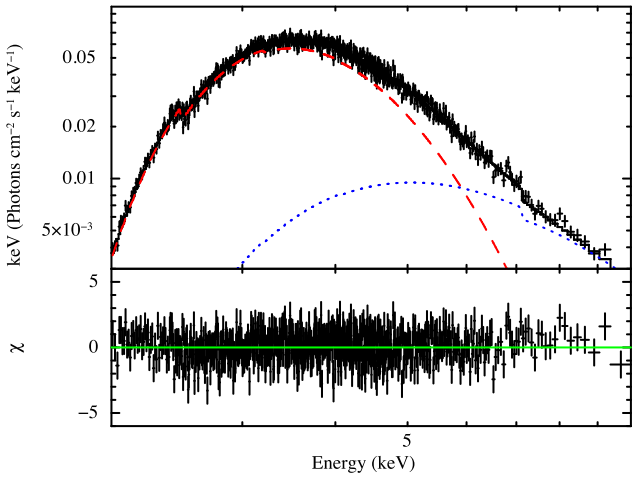

Figure 5. (Upper panel) EPIC-pn mean spectrum fitted with a blackbody plus thermal Comptonization component, all absorbed by neutral material. The red dashed and blue dotted lines show the contribution from the blackbody and thermal Comptonization components, respectively (see Table 3). (Lower panel) Residuals compared to the best-fitting model.

5 LONG-TERM SPECTRAL VARIATIONS

5.1 The Swift monitoring

We first fitted all *Swift* spectra with an absorbed power-law model DUST*TBNEW*POWERLAW. Due to the lower statistics of the single ∼1 ks *Swift* spectra, we assumed a column density of $N_{\rm H} = 25.6 \times 10^{22}$cm^{-2} (see Table 2) as found in fitting the higher resolution *XMM–Newton* EPIC spectra. This model cannot satisfactorily reproduce all spectra, especially when Swift J174540.7−290015 enters softer states. Nevertheless, by applying this simple model we can probe the evolution of the spectral shape by tracking the variations of the power-law photon index. Fig. 6 shows the best-fitting power-law photon index to the 2–10 keV band. We observe a gradual steepening of the spectral shape with time. In

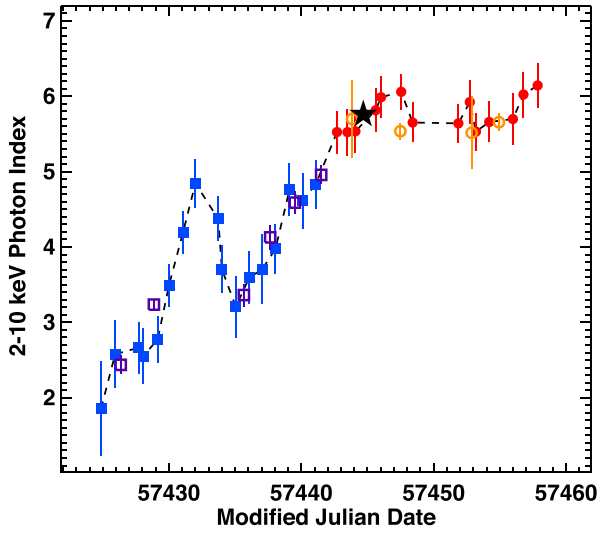

Figure 6. Spectral slope evolution of Swift J174540.7−290015. Colour symbols have the same meaning as in Fig. 7. The photon indices are derived by fitting an absorbed power law to the 2–10 keV spectrum of every observation, separately, assuming $N_{\rm H} = 25.6 \times 10^{22}$ cm^{-2} from fitting the *XMM–Newton* spectra. The square symbols indicate the hard-state observations (filled blue – PC mode, empty purple – WT mode), while the circular symbols indicate the soft-state observations (filled red – PC mode, empty orange – WT mode). The black star indicates the *XMM–Newton* observation.

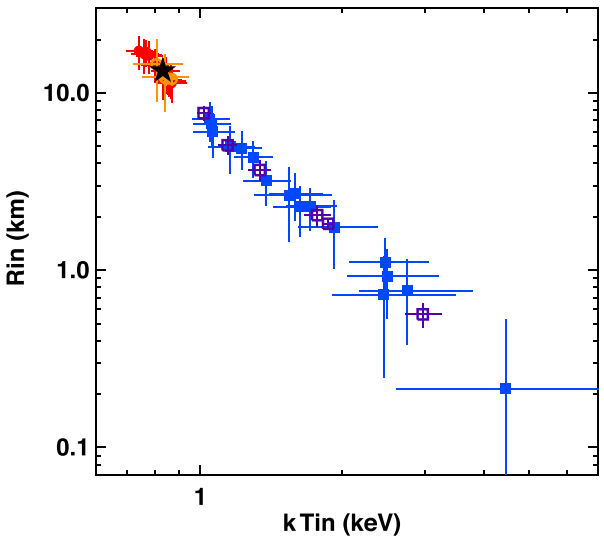

Figure 7. The inner disc temperature and flux derived from the best-fitting disc blackbody model to the spectrum in every *Swift* observation (with $N_{\rm H}$ fixed at 15.9×10^{22} cm^{-2}). The square symbols indicate the hard-state observations (filled blue – PC mode, empty purple – WT mode), while the circular symbols indicate the soft-state observations (filled red – PC mode, empty orange – WT mode). The black star indicates the *XMM–Newton* observation.

particular, very steep spectral shapes (with $\Gamma > 5$) are observed in the later observing period. Such steep spectral indices might indicate a thermal nature of the emission mechanism. Therefore, we then fitted all the *Swift* spectra with an absorbed multitemperature disc blackbody model (DUST*TBNEW*DISKBB). Fig. 7 shows the best-fitting inner disc temperature versus the inner disc radius. A Kendall's rank correlation test provides a correlation coefficient of $\rho = -0.95$ and null hypothesis probability of 7×10^{-25}. Despite its significance, we think that this anticorrelation is induced by fitting the data with the wrong spectral model. Indeed, we note that (i) the spectra accumulated before MJD = 57442 (blue filled and violet open squares in Figs 6 and 7) are better fit by a power-law component; (ii) the best-fitting inner disc radii of these spectra is significantly smaller than 10 km, implying that the accretion disc extends either inside the NS surface or inside the event horizon of a stellar mass BH during these observations. On the other hand, all the *Swift* spectra after MJD = 57442 (red filled and orange open points in Figs. 6 and 7) are well fitted by this absorbed thermal emission model. However, these relatively low S/N spectra cannot rule out the presence of an additional component in the hard X-ray as observed by *XMM–Newton*. In Fig. 7, the orange open and red filled points cluster around a small parameter space, indicating that these spectra also have similar shape. Moreover, this model cannot reproduce the spectra when there is clearly a hard component, as represented by the blue and purple squares in Fig. 7. Fitting these spectra requires a very high temperature ($kT \sim$ 1–8 keV) of the thermal component and variations of the normalization that imply unlikely variations of the thermal emitting area (see Fig. 7).

Finally we adopt model 2 of Table 3 that is composed by the sum of a thermal multitemperature disc blackbody component plus a power-law (DUST*TBNEW*(DISKBB+POWERLAW)). This model can well produce all the *Swift* spectra. From top to bottom, Fig. 8 shows the source flux, in the 2–5, 5–8 and 2–8 keV band as well as the hardness ratio plotted against the observation date. During the first few days of *Swift* observations, Swift J174540.7−290015 showed a clear and significant flux increase, by a factor of 3–4. Very significant variability, stronger in the hard band, and a hard X-ray spectrum are observed up to MJD = 57442 (see Fig. 8). Afterwards, the spectrum softens, with a hardness ratio HR < -0.5 and no strong variability is observed anymore (see Fig. 8).

To enhance the S/N, we combined[3] the *Swift* spectra obtained before and after MJD = 57442. The combined spectra of these two periods are shown in Fig. 9 with blue and red symbols, respectively. To capture what are the bulk of the spectral variations and to avoid model degeneracies (as demonstrated by the higher statistic *XMM–Newton* spectrum), we consider here only a single emission component model. The spectral degeneracy will be broken by the addition of the *INTEGRAL* data, above 10 keV. The hard-state spectrum is better fit ($\chi^2 = 613$ for 538 dof) by a simple absorbed power-law model with spectral index of $\Gamma = 2.56 \pm 0.07$ ($N_{\rm H} = 17.2 \pm 0.5 \times 10^{22}$ cm^{-2}). A fit with either a single blackbody or multitemperature disc blackbody component provides a significantly worse fit ($\Delta\chi^2 = 141$ and 56, respectively). The combined soft-state spectrum is fit by a simple absorbed multitemperature disc blackbody component with best-fitting temperature $kT_{\rm in} = 0.80 \pm 0.02$ keV ($N_{\rm H} = 16.8 \pm 0.7 \times 10^{22}$ cm^{-2}, $\chi^2 = 374$ for 329 dof) and inner disc radius of $r_{\rm in} = 15 \pm 2$ km. This value is fully compatible with what is expected by an accreting NS or a BH. Note that the best-fitting temperature is slightly lower than the

[3] We use the ADDSPEC tool in the FTOOLS 6.18 package to derive the combined source and background spectra, and group them with GRPPHA. Note that some observations with short exposure and thus very few counts are excluded from the spectral combination. These low S/N spectra cannot improve the combined spectra much, and the inclusion of these spectra would also cause extra empty bins in the combined spectra due to the spectral combining algorithm. We also note that the different observations caught Swift J174540.7−290015 at different fluxes and hardness ratios, therefore limiting the power of extracting detailed spectral information from these averaged spectra.

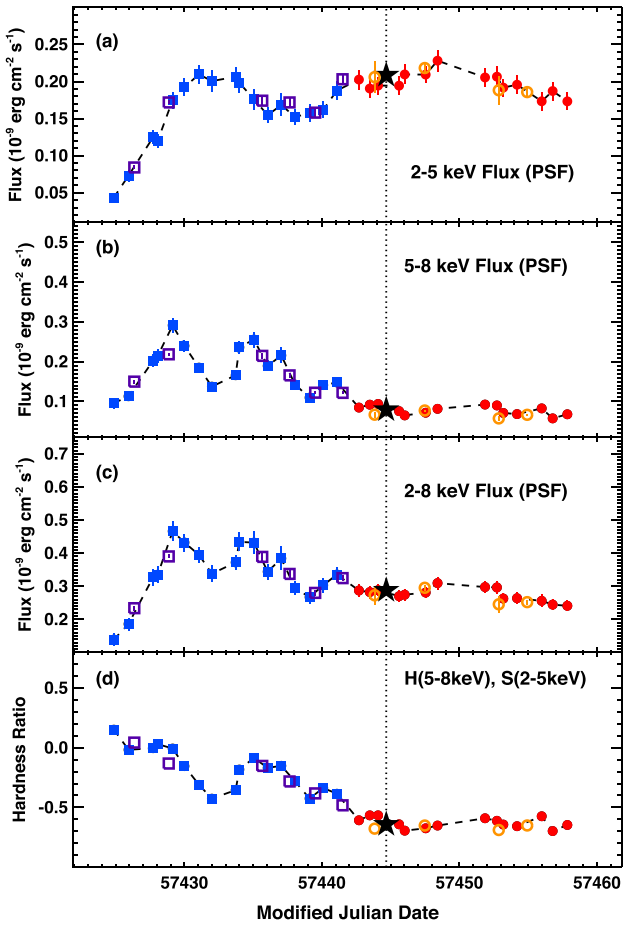

Figure 8. Panels a, b and c are the PSF-corrected *Swift* XRT flux of Swift J174540.7−290015 in the 2–5 keV, 5–8 keV and 2–8 keV band, respectively. The blue filled square symbols correspond to the PC mode observations when the source spectrum is dominated by a hard X-ray power-law component. The purple empty squares represent the data in WT mode. The red filled circular symbols correspond to the observations when the source spectrum is dominated by a soft X-ray thermal component (see Figs 7 and 9). The orange empty squares represent the data in WT mode. Panel d shows the hardness ratio between the hard band (5–8 keV) and soft band (2–5 keV). In all panels, the black star and the dashed line indicate the *XMM–Newton* observation on 2016 February 26.

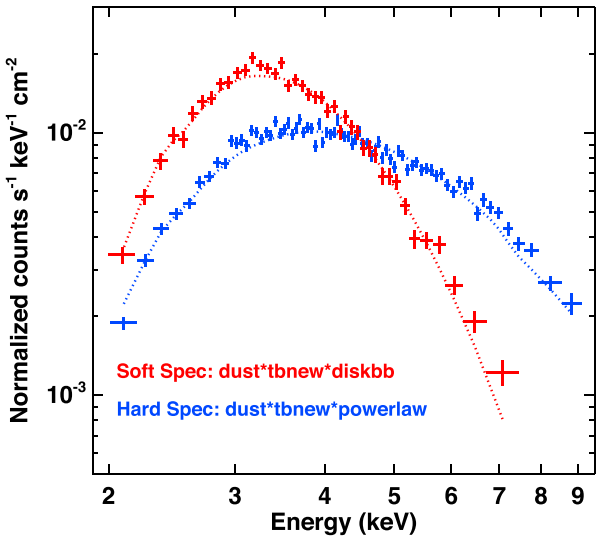

Figure 9. Combined, background-subtracted, *Swift* XRT spectra of the soft-state (red) and hard-state (blue) periods. The combined soft-state spectrum is well fitted by an absorbed disc blackbody ($N_{\rm H} = 16.8 \times 10^{22}$ cm^{-2}, $kT_{\rm in} = 0.80$ keV), while the hard state by an absorbed power-law component ($N_{\rm H} = 17.2 \times 10^{22}$ cm^{-2}, $\Gamma = 2.56$).

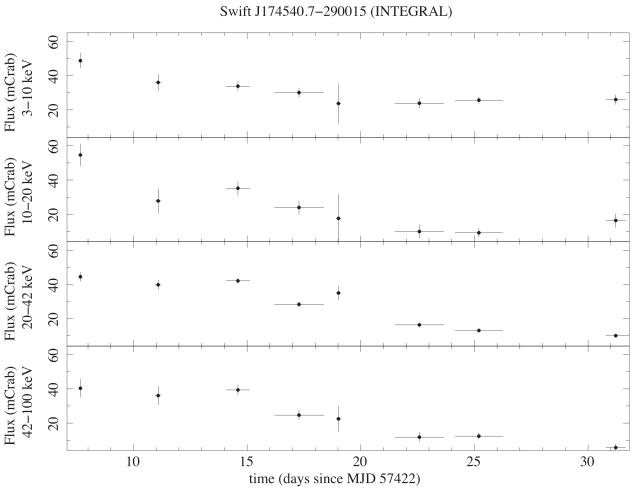

Figure 10. JEM-X and IBIS/ISGRI light curves of Swift J174540.7−290015 in different energy bands. Each point is integrated for both instruments over an entire *INTEGRAL* revolution (from 1643 to 1652). The state transition inferred from the *Swift* data occurred around day 20. The *INTEGRAL* data show a simultaneous significant drop of hard X-ray emission ($E > 10$ keV), further confirming this interpretation.

mean value in Fig. 7, which is because the column density of neutral material ($N_{\rm H}$) is allowed to vary when fitting the combined spectra. For the soft-state combined spectrum, a fit with an absorbed power law provides a slightly better fit ($\chi^2 = 353$ for 329 dof); however, the suspiciously large best-fitting spectral index ($\Gamma = 5.83 \pm 0.18$, $N_{\rm H} = 26.2 \pm 1.0 \times 10^{22}$ cm^{-2}) disfavours this interpretation and leaves the disc blackbody model as the more physical interpretation. The marked spectral and variability difference before and after MJD = 57442 is reminiscent of spectral transitions in accreting X-ray binaries (Fender, Belloni & Gallo 2004; Remillard & McClintock 2006), and it suggests that Swift J174540.7−290015 might have undergone a state transition during the *Swift* monitoring campaign.

5.2 The INTEGRAL monitoring

To break the degeneracies in the *XMM–Newton* and *Swift* data, induced by the limited energy band considered, we investigated the source behaviour in the *INTEGRAL* energy band. Fig. 10 shows the JEM-X and IBIS/ISGRI light curves of Swift J174540.7−290015, since the start of the outburst. The source is detected in all energy bands. In particular, a significant drop of hard X-ray emission ($E > 10$ keV) is observed after day 20, in correspondence to the state transition inferred from the *Swift* data (Fig. 10), therefore, further confirming this scenario (see Section 5.1).

We accumulated all *INTEGRAL* data that are quasi-simultaneous to *Swift* observations and we created a combined 'hard-state' and 'soft-state' spectrum (summing all ISGRI and JEM-X spectra from revolution 1643–1648 and 1649–1652, corresponding to MJD 57429–57441 and 57443–57453, respectively). We then performed a broad-band fit by considering these *INTEGRAL* and *Swift* spectra. As already clear from the analysis of the *XMM–Newton* and

Table 4. Best-fitting parameters of the combined, nearly simultaneous *INTEGRAL* and *Swift* soft-state and hard-state spectra of Swift J174540.7−290015. The same models applied to the higher statistics *XMM–Newton* spectrum have been fitted to the combined broad-band soft-state (1S, 2S and 4S) spectrum, as well as to the hard-state (1H, 2H) one. For the definition of the units of all the other parameters, see Tables 2 and 3.

	Broad band fit of composite soft- and hard-state spectra ABS = DUST*TBNEW				
		Composite soft state		Composite hard state	
	ABS*(DISKBB+BBODY)	ABS*(BBODY+NTHCOMP)	ABS*(DISKBB+NTHCOMP)	ABS*(DISKBB+NTHCOMP)	ABS*(BBODY+NTHCOMP)
Model	(4S)	(1S)	(2S)	(2H)	(1H)
$N_{\rm H}$	15.9 ± 0.9	17.1 ± 1.1	18.8 ± 1.0	14.3 ± 1.0	13.3 ± 1.0
$kT_{\rm BB}$	0.62 ± 0.02	0.57 ± 0.03			0.79 ± 0.1
$A_{\rm BB}$	1100 ± 350	1800 ± 800			68^{+63}_{-23}
$kT_{\rm DBB}$	$10^{2.6}_{-1.6}$		0.67 ± 0.04	1.16 ± 0.18	
$A_{\rm DBB}$	$1^{+1.2}_{-0.5} \times 10^{-3}$		1100^{+700}_{-400}	14^{+21}_{-8}	
Γ		2.1 ± 0.4	2.1 ± 0.4	1.92 ± 0.05	1.94 ± 0.06
A_Γ		$1.4^{+1.0}_{-0.5} \times 10^{-2}$	$2.9 \pm 1.7 \times 10^{-2}$	$8.7 \pm 5 \times 10^{-3}$	$2.4 \pm 1 \times 10^{-3}$
$C_{\rm JEMX1}$	<1.16	0.96 ± 0.2	0.96 ± 0.2	1.5 ± 0.2	1.5 ± 0.1
$C_{\rm JEMX2}$	<1.04	$1.3^{+1.5}_{-0.7}$	$1.4^{+1.6}_{-0.7}$	$0.98^{+0.18}_{-0.13}$	0.92 ± 0.12
$C_{\rm ISGRI}$	<1.06	0.89 ± 0.18	0.9 ± 0.2	0.85 ± 0.12	0.70 ± 0.12
χ^2/dof	369.5/331	357.0/331	355.9/331	648.9/552	659.2/552

Swift data, a single component emission model is not an adequate description of the emission of Swift J174540.7−290015 (see Sections 4.1 and 5.1). Therefore, we began by applying the best-fitting double component models fitting the *XMM–Newton* spectrum (see Table 3) to the soft-state cumulative *Swift* and *INTEGRAL* spectra. In all models that we explored, we applied an inter-normalization factor (see Table 4) between the different instruments.

We first considered the absorbed double thermal component [CONS*ABS*(DISKBB+BBODY), see model 4 in Table 3]. This model (see Section 4.1 and Table 3), being composed by two thermal components peaking below 2 keV, predicts very little emission above ∼20 keV. On the contrary, even in the soft state, Swift J174540.7−290015 emits significant radiation above 20 keV. To try to reproduce the hard X-ray emission, this model increases the best-fitting temperature of the disc blackbody component and lowers the disc inner radius to unrealistic values. Indeed, the best-fitting temperature is $kT_{\rm DBB} = 10^{+2.6}_{-1.6}$ keV and the inner disc radius is $r_{\rm in} \sim 0.025$ km, the latter being too small for either an NS or a BH. For this reason we rule out this model.

We then tested the absorbed blackbody plus Comptonization component [CONS*ABS*(BBODY+NTHCOMP), model 1 in Table 3] as well as the absorbed disc blackbody plus Comptonization component [CONS*ABS*(DISKBB+NTHCOMP) model 2 in Table 3]. Incidentally, we note that even adding the *INTEGRAL* data, the energy of the cutoff in the electron distribution is unconstrained ($E > 15$ keV). Therefore, we fix this value to 50 keV, as in the previous fits (Section 4.1 and Table 3). Both these thermal plus Comptonization models provide a good description of the data ($\chi^2 = 357.0$ for 331 dof, $\chi^2 = 355.9$ for 331 dof, respectively). We note that the best-fitting parameters of the absorber, blackbody and disc blackbody components are consistent with the ones obtained by fitting the higher statistics *XMM–Newton* spectrum alone (see Table 3). However, the addition of the *INTEGRAL* data allows us to obtain now more reliable constraints on the parameters of the Comptonization component. In particular, the photon index of the Comptonization component ($\Gamma = 2.1$) is now consistent with the values typically observed in accreting compact objects. Moreover, the detection of X-ray emission up to ∼50 keV, allowed us to rule out that the soft-state emission is only composed by a combination of pure thermal components.

We then also fitted the combined hard-state spectrum (see Fig. 11). The broad-band spectra can be fit by an absorbed Comptonization component plus either a blackbody or a disc blackbody (see models 1H and 2H in Table 4). None of these two models provide a completely acceptable fit ($\chi^2 = 659.2$ for 552 dof and $\chi^2 = 648.9$ for 552 dof, respectively). We attribute this to the strong spectral and flux evolution (e.g. variation in photon index) observed during the hard state (see Section 5.1), that cannot be properly taken into account by the fit of these combined spectra. Therefore, we refrain the reader from extracting too detailed information from these spectra.[4] It is clear, however, that the hardness ratio changed by a factor of ∼3.4 between the hard ($F_{\rm H_{10-100\,keV}} = 6.5 \times 10^{-10}$ erg cm^{-2} s^{-1}, $F_{\rm H_{2-10\,keV}} = 3.8 \times 10^{-10}$ erg cm^{-2} s^{-1}) and soft ($F_{S_{10-100\,keV}} = 1.4 \times 10^{-10}$ erg cm^{-2} s^{-1}, $F_{S_{2-10\,keV}} = 2.8 \times 10^{-10}$ erg cm^{-2} s^{-1}) state (see Fig. 11). This reinforces the interpretation that the source underwent a state change during the monitored period.

6 POSSIBLE NEAR-IR COUNTERPART

The location of Swift J174540.7−290015 was observed with the GROND (Greiner et al. 2008) instrument mounted at the MPG/European Southern Observatory 2.2 m telescope in La Silla, on 2016 February 19.35 UT. Observations were obtained simultaneously in the *J*, and *H* photometric bands for 640 s integration time each[5]. The data were reduced with the standard tools and methods as described in Krühler et al. (2008). The photometry was measured from circular apertures with radii corresponding to the image full width at half-maximum (1.1 arcsec in *J* and 1.4 arcsec in *H*) and calibrated against 2MASS stars in the same field.

A single bright source, reported also by Masetti et al. (2016) from archival VISTA Variables in the Via Lactea (VVV) imaging, is seen at the *Chandra* X-ray position. The apparent aperture magnitudes (in the Vega system) are $J = 15.97 \pm 0.12$ and $H = 12.76 \pm 0.13$. The location of the new transient was also contained in a series of 15 GROND observations obtained on 2015 April 26.35–26.42 UT when monitoring another GC transient. No variability was found for the bright near-IR source in the *J* or *H* band during this set

[4] For example, we note that some inter-normalization factors are not consistent with 1 and that significant residuals are still present.

[5] GROND observes simultaneously in g', r', i', z', J, H, K. Due to the extreme Galactic foreground reddening affecting the optical bands and saturation affecting the *K* band, only the *J*- and *H*-band data are discussed here.

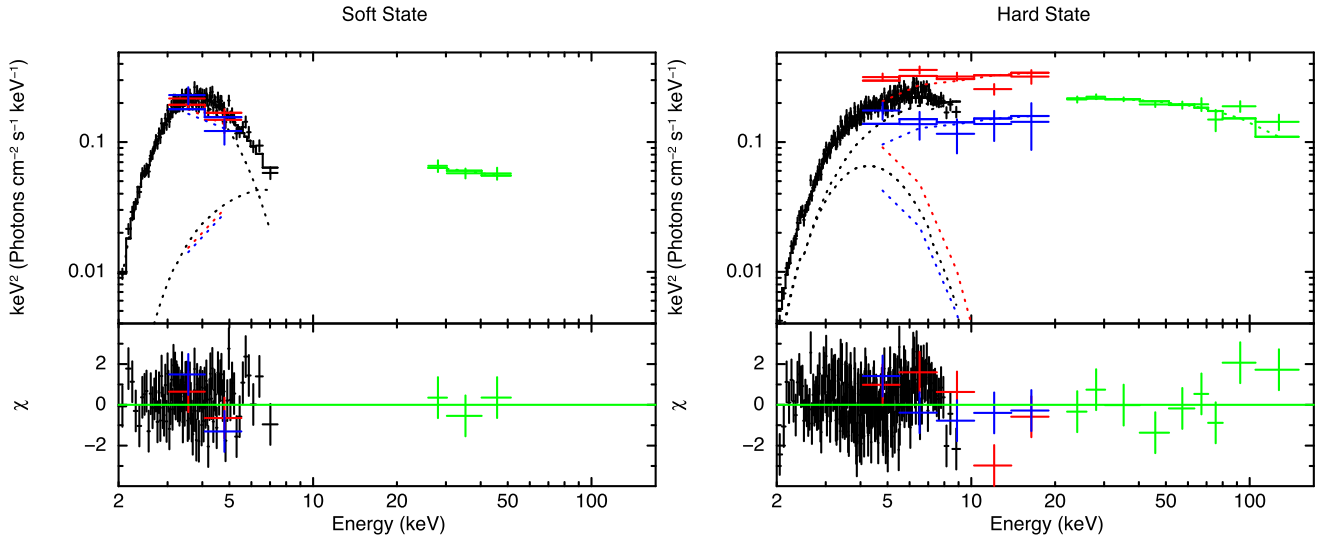

Figure 11. The broad-band spectra of Swift J174540.7−290015 extracted during the soft and hard states (as defined in Section 5.2). For the hard state (right-hand panel), we used data from the *INTEGRAL* revolutions 1643–1648 (in black, red, blue and green are the *Swift* XRT, JEM-X1, JEM-X2 and IBIS/ISGRI). For the soft state (left panel), data from revolutions 1649–1652 have been used (same colour scheme as before). The soft-state spectrum is dominated by an absorbed thermal component below ∼10 keV and a Comptonization tail at higher energies. The hard-state spectrum is dominated by an absorbed Comptonization component inducing significantly larger high energy flux. See text for details.

of observations and the median magnitudes of $J = 16.10 \pm 0.11$ (seeing 1.1 arcsec) and $H = 12.57 \pm 0.10$ (1.6 arcsec) are consistent within errors with the post-outburst measurements.

The near-IR source density at the position of the transient is very high and GROND photometry corresponds with the co-addition of the flux of all sources within the aperture. Therefore, we can only conclude, that the brightest source within the *Chandra* error circle, dominating the total emission, remained constant between the pre- and post-outburst observations and none of the fainter objects brightened to a level, where it would increase the overall emission within the aperture by more than 0.1 mag.

The GC is routinely observed with adaptive optics using *NaCo* at the VLT (see Gillessen et al. 2009, for a description of the program and data reduction). Fig. 12 shows a stacked *NaCo K*-band image from archival (pre-outburst) observations. Besides the bright source dominating the GROND photometry, multiple fainter objects are resolved either inside or in the close proximity to the *Chandra* error region (black circle). For the bright source (see Fig. 12), we measure magnitudes of $H = 12.98 \pm 0.06$ and $K = 10.81 \pm 0.03$, while, for comparison, the fainter star (indicated with 2 in Fig. 12) has $H_{\rm star2} = 17.24 \pm 0.06$ and $K_{\rm star2} = 15.23 \pm 0.03$. The MPE-IR group obtained new *NaCo* data on 2016 March 16. No significant variation in brightness of any of the sources within the *Chandra* error circle is observed (Gillessen private communication).

The probability of having such a bright star within the *Chandra* error circle of ∼0.4 arcsec^2 can be computed from number of stars with $m_{\rm Ks} > 11$ mag within an annulus centred on Sgr A* and with inner and outer radii of $16 - 5$ arcsec and $16 + 5$ arcsec, respectively. This annulus includes the position of the putative near-IR counterpart. The observed surface density within the annulus is 0.032 stars arcsec^{-2} implying a chance coincidence probability of ∼1 per cent of finding a source with $m_{\rm Ks} > 11$ mag within the *Chandra* error circle, i.e. that the bright source is not associated with the X-ray transient.

Using the average reddening towards the GC of $A_{\rm K} = 2.4 \pm 0.1$ mag (Fritz et al. 2011), the absolute *K*-band magnitude is $M_{\rm K} = -6.1$. The star spectroscopically

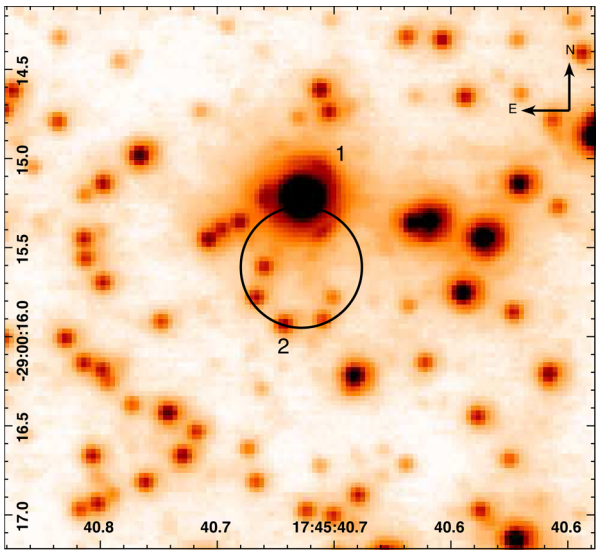

Figure 12. VLT-*NaCo* archival K-band image of the field of Swift J174540.7−290015. The *Chandra* error circle (Baganoff et al. 2016) is shown by the black circle, with 0.34 arcsec radius. The bright candidate counterpart (1) as well as a fainter one (2) are indicated. See text for details. North is up, and east is left.

shows the CO band heads in the *K* band, which excludes stars hotter than spectral class F (Wallace & Hinkle 1997). The absolute magnitude would suggest it to be a late-type giant or supergiant.

7 DISCUSSION

We report the identification of a new accreting X-ray binary, Swift J174540.7−290015 and results from the early phases of its X-ray emission evolution. Swift J174540.7−290015 reached a peak flux at an absorbed value of $F = 6 \times 10^{-10}$ erg cm^{-2} s^{-1} in the 2–10 keV band. During the *XMM–Newton* observation, Swift J174540.7−290015 shows an absorbed and un-absorbed 2–10 keV

flux of $F_{\rm abs} = 2.9 \times 10^{-10}$ and $F_{\rm un\text{-}abs} = 14.5 \times 10^{-10}$ erg cm^{-2} s^{-1}, respectively, that corresponds to $F_{\rm un\text{-}abs} = 52.8 \times 10^{-10}$ erg cm^{-2} s^{-1} in the 0.1–10 keV band. During the *XMM–Newton* observation, Swift J174540.7−290015 showed an observed 2–10 keV luminosity of $L_{\rm abs} = 2.1 \times 10^{36}$ erg s^{-1} and an un-absorbed luminosity of $L_{\rm un\text{-}abs} = 3.8 \times 10^{37}$ erg s^{-1} in the 0.1–10 keV band. Therefore, if Swift J174540.7−290015 is an NS with $M_{\rm NS} = 1.4$ M$_\odot$, the observed luminosity is $L \sim 20$ per cent of the Eddington limit during the *XMM–Newton* observation ($L < 20$ per cent if Swift J174540.7−290015 is a BH). Given these luminosities, Swift J174540.7−290015 does not belong to the class of faint X-ray transients (Wijnands et al. 2006).

We point out that Swift J174540.7−290015 is located at less than 16 arcsec from Sgr A* (the supermassive BH at the GC), less than 17 arcsec from SGR J1745−2900 (Mori et al. 2013; Rea et al. 2013; Coti Zelati et al. 2015) and less than 1.7 arcmin from the NS LMXB AX J1745.6−2901 (Ponti et al. 2015b, 2016), therefore it lies in the field of view of all *XMM–Newton* observations pointed to one of these sources (Ponti et al. 2015a, Ponti et al. 2015b,2015d, 2016). No evidence for previous outbursts of Swift J174540.7−290015 is present in the *XMM–Newton*, *Chandra* and *Swift* archive (Degenaar et al. 2012; Ponti et al. 2015a, Ponti et al. 2015b).

We compute the upper limit on the X-ray emission of Swift J174540.7−290015 during quiescence by stacking all *Chandra* ACIS-I observations between 1999 and 2011, for a total exposure of ∼1.8 Ms. We observe 54 counts within 0.34 arcsec from the position of Swift J174540.7−290015, in the 0.5–10 keV band. This translates in a 95 per cent upper limit of 3.5×10^{-5} cts s^{-1} (Gehrels 1986). Assuming the quiescent spectrum of Swift J174540.7−290015 is described either by an absorbed ($N_{\rm H} = 18.7 \times 10^{22}$ cm^{-2}) power law (with spectral index $\Gamma = 2$) or a blackbody ($kT_{\rm BB} = 0.3$ keV) this can be translated into an un-absorbed luminosity of $L_{\rm PL_{0.5-10}} < 5 \times 10^{31}$ erg s^{-1} or $L_{\rm BB_{0.5-10}} < 1.7 \times 10^{33}$ erg s^{-1}. This upper limit on the quiescent X-ray luminosity is consistent with both an NS or BH origin of Swift J174540.7−290015 (Narayan, Garcia & McClintock 1997; Garcia et al. 2001; Rea et al. 2011; Armas Padilla et al. 2014).

Radio observations did not detect either a steady or periodic counterpart to Swift J174540.7−290015. Steady emission is expected under two scenarios. First, the Fundamental Plane of BH activity can be used to predict the radio luminosity under the assumption that the system is in the low hard state (Plotkin et al. 2012). For a 10 M$_\odot$ BH with the unabsorbed X-ray luminosity observed by *XMM–Newton*, we predict a radio flux density of 6 mJy. The scatter in the Fundamental Plane is approximately an order of magnitude so that values as high as 100 mJy are possible. The imaging non-detection with an rms of 6 mJy, thus, can neither rule out nor confirm the presence of a jet in this system. We note that by the time the first VLA observation has been taken, Swift J174540.7−290015 already transitioned to the soft state. Secondly, bright radio emission can be produced through interaction of a jet with the dense ISM of the GC. The LMXB CXOGC J174540.0−290031, located only 0.1 pc in projection from Sgr A*, reached a peak flux density of 100 mJy that was resolved into two lobes on either sides of the X-ray (Bower et al. 2005). The proximity of Swift J174540.7−290015 to Sgr A West suggests that it could produce similar interactions but we find no evidence for these.

The emission of Swift J174540.7−290015, during the *XMM–Newton* observation is dominated by a thermal component that can be well fitted either by multitemperature disc blackbody, or blackbody emission. In addition, emission at higher energies (up to 20–50 keV) is clearly detected by *INTEGRAL*. The high energy emission is a clear sign of a Comptonization component, ruling out a double thermal component consistent with the fits limited to energies below 10 keV. The disc blackbody plus Comptonization scenario is perfectly compatible either with an NS or BH primary. In this framework, the Comptonization component might be associated with the coronal emission typically observed in accreting sources and the multitemperature disc blackbody could be produced by a standard accretion disc extending down to ∼6.5 r$_{\rm S}$ for an NS ($M_{\rm NS} = 1.4$ M$_\odot$) or ∼2 r$_{\rm S}$ for a BH with $M_{\rm BH} = 5$ M$_\odot$. In the second scenario (model 1 and 1S in Table 3 and 4, respectively), the presence of the blackbody emission suggests that the primary is an NS. Also in this scenario, the Comptonization might be due to coronal emission, but the soft radiation would be dominated by the boundary layer emission. However, the best-fitting blackbody radius appears to be too large ($R_{\rm BB} = 35 \pm 11$ km) to be associated with a conceivable NS. Nevertheless, we cannot exclude that the large observed area, attributed to the blackbody emission, might be induced by the contribution from a disc emission component not considered in our modelling. Alternatively, the blackbody component might be in part produced by hotspots on the surface of the NS. Would this indeed be the case, then a pulsation should be present. However, this pulsation might be undetected either because of the weakness of the blackbody emission or because Swift J174540.7−290015 is a fast spinning millisecond pulsar (e.g. faster than our timing resolution, or a weak signal possibly also smeared by a Doppler orbital shift).

From the spectral behaviour of Swift J174540.7−290015, we can rule out a high-mass X-ray binary (HMXB) nature of the source. The spectra of HMXBs are characterized by a dominant hard power law in the 0.2−10.0 keV band with typical photon indices of 1.0−1.5 for supergiant systems and around 0.9 for Be/X-ray binaries (e.g. Haberl, Eger & Pietsch 2008; Bodaghee et al. 2012; Bozzo et al. 2012; Walter et al. 2015). HMXBs also do not show spectra state transitions as observed from Swift J174540.7−290015.

Swift J174540.7−290015 was initially identified as a possible magnetar due to its fast outburst rise. However, many observational characteristics of this new transient are at variance with what is usually observed in magnetar outbursts (see Rea & Esposito 2011 and Turolla, Zane & Watts 2015, for a review on outbursts and on magnetars in general, respectively). The strong variability of the outburst flux decay (see Fig. 8) is unseen in the outburst decay of magnetars, which are usually observed to decay smoothly towards quiescence. This is also in line with the interpretation of these outbursts as being due to a large energy injection in the magnetar crust triggered by the instability of the internal or external magnetic field (possibly by a strongly twisted magnetic bundle), with a consequent crustal heating and subsequent cooling (Beloborodov 2009; Pons & Rea 2012). Furthermore, if placed at 8 kpc, the peak luminosity of the outburst is too high with respect to what is observed for magnetars, $L_X < 10^{36}$ erg s^{-1}, which is a limit believed to be regulated by the strong dependence on temperature of the crustal neutrino emissivity (Pons & Rea 2012). The deep upper limits on the PF of this new transient (see Fig. 4) are rather unlikely (although a few exceptions exists) compared with the usual strength (∼20–80 per cent) of the periodic signals (around 2–10 s) observed for magnetars. Therefore, we believe the magnetar interpretation for this new transient is extremely unlikely.

Observations of the X-ray reflection nebulae (irradiated molecular clouds within a few hundred parsecs from Sgr A*) suggest an either Solar or supersolar Iron abundance of the GC ISM (Revnivtsev et al. 2004; Ponti et al. 2010, Ponti et al. 2013, Ponti et al.

2014a; Terrier et al. 2010; Zhang et al. 2015). The observed low iron abundance ($A_{\rm Fe} = 0.5 \pm 0.4$ Solar) of the neutral absorbing material towards Swift J174540.7−290015 is therefore rather surprising also with respect to the accepted iron gradient in the Galactic disc (Friel et al. 2002; Pedicelli et al. 2009). We note that the measured value is consistent with the iron abundance towards 4U 1820–303, an X-ray binary located at a distance of ∼7.6 kpc, at less than 1 kpc from the GC (towards $l = 2.^{\circ}79$ and $b = -7.^{\circ}91$; Kuulkers et al. 2003; Pinto et al. 2010). The observed under abundance is also in line with the values measured towards a small sample of bright Galactic X-ray binaries (Juett et al. 2006). We attribute this to depletion of iron into dust grains in the ISM (see Juett et al. 2006). Indeed, depletion of elements in dust grains can reduce the effective cross-section for absorption. In grains, the optical depth can be higher than 1, therefore absorption will occur primarily on the surface. Moreover, iron atoms located deeper into the grain will be shielded and they will not contribute to the absorption, effectively reducing the strength of the element absorption edge (e.g. Juett et al. 2006). The similarity of the observed iron abundance to the ones measured along many other line of sights, is consistent with the idea that a significant fraction of the absorption is produced in the ISM along the Galactic arms and therefore it does not carry information about the metal abundances characteristic of the GC region. Future detailed modelling of the dust scattering halo of AX J1745.6−2901 and Swift J174540.7−290015 will better constrain this.

Given the long-term X-ray variability and spectral decomposition, we then identify Swift J174540.7−290015 as an accreting X-ray binary hosting an NS or a BH, most likely with a low-mass star companion. The discovery and identification of this new GC transient as well as the continuous X-ray monitoring of the central parsec is improving the determination of the population of stellar remnants orbiting Sgr A⋆.

ACKNOWLEDGEMENTS

The authors wish to thank N. Schartel and the *XMM–Newton* team for performing the *XMM–Newton* observation and the 'MPE-IR-group Galactic Centre team' for sharing the reduced, cleaned, calibrated *NaCo* images and photometry as well as for help with the interpretation and discussion. The GC *XMM–Newton* monitoring project is supported by the Bundesministerium für Wirtschaft und Technologie/Deutsches Zentrum für Luft- und Raumfahrt (BMWI/DLR, FKZ 50 OR 1408) and the Max Planck Society. The National Radio Astronomy Observatory is a facility of the National Science Foundation operated under cooperative agreement by Associated Universities, Inc. NR and FCZ acknowledge financial support from a Dutch NWO Vidi grant. NR also acknowledges support from Spanish grants AYA2015-71042 and SGR2014-1073. This research has made use primarily of data obtained with *XMM–Newton*, an ESA science mission with instruments and contributions directly funded by ESA Member States and NASA, and on data obtained from the *Swift* Data Archive. Part of the funding for GROND (both hardware as well as personnel) was generously granted from the Leibniz-Prize to Prof. G. Hasinger (DFG grant HA 1850/28-1). The authors would like to thank P. Wiseman, J. Greiner (both MPE) and A. Hempel (PUC) for their support with the GROND observation.

REFERENCES

Anders E., Grevesse N., 1989, Geochim. Cosmochim. Acta, 53, 1197
Armas Padilla M., Wijnands R., Degenaar N., Muñoz-Darias T., Casares J., Fender R. P., 2014, MNRAS, 444, 902
Baganoff F. K. et al., 2016, The Astron. Telegram, 8746
Beloborodov A. M., 2009, ApJ, 703, 1044
Bodaghee A., Tomsick J. A., Rodriguez J., Chaty S., Pottschmidt K., Walter R., Romano P., 2012, AIP Conf. Ser., Vol. 1427, SUZAKU 2011: Exploring the X-ray Universe: Suzaku and Beyond. Am. Inst. Phys., New York, p. 52
Bower G. C., Roberts D. A., Yusef-Zadeh F., Backer D. C., Cotton W. D., Goss W. M., Lang C. C., Lithwick Y., 2005, ApJ, 633, 218
Bower G. C. et al., 2016, The Astron. Telegram, 8793
Bozzo E., Pavan L., Ferrigno C., Falanga M., Campana S., Paltani S., Stella L., Walter R., 2012, A&A, 544, A118
Bozzo E. et al., 2016, A&A, 589, A42
Campana S., 2009, ApJ, 699, 1144
Coti Zelati F. et al., 2015, MNRAS, 449, 2685
Courvoisier T. J.-L. et al., 2003, A&A, 411, L53
De Marco B., Ponti G., Muñoz-Darias T., Nandra K., 2015, MNRAS, 454, 2360
Degenaar N., Wijnands R., Cackett E. M., Homan J., in't Zand J. J. M., Kuulkers E., Maccarone T. J., van der Klis M., 2012, A&A, 545, A49
Degenaar N., Wijnands R., Miller J. M., Reynolds M. T., Kennea J., Gehrels N., 2015, J. High Energy Astrophys., 7, 137
Dexter J., O'Leary R. M., 2014, ApJ, 783, L7
Díaz Trigo M., Parmar A. N., Boirin L., Méndez M., Kaastra J. S., 2006, A&A, 445, 179
Eatough R. P. et al., 2013, Nature, 501, 391
Esposito V. et al., 2016, The Astron. Telegram, 8684
Faucher-Giguère C.-A., Loeb A., 2011, MNRAS, 415, 3951
Fender R., Belloni T., 2012, Science, 337, 540
Fender R. P., Belloni T. M., Gallo E., 2004, MNRAS, 355, 1105
Frank J., King A. R., Lasota J.-P., 1987, A&A, 178, 137
Friel E. D., Janes K. A., Tavarez M., Scott J., Katsanis R., Lotz J., Hong L., Miller N., 2002, AJ, 124, 2693
Fritz T. K. et al., 2011, ApJ, 737, 73
Garcia M. R., McClintock J. E., Narayan R., Callanan P., Barret D., Murray S. S., 2001, ApJ, 553, L47
Gehrels N., 1986, ApJ, 303, 336
Genzel R. et al., 2010, MNRAS, 407, 2091
Gillessen S., Eisenhauer F., Fritz T. K., Bartko H., Dodds-Eden K., Pfuhl O., Ott T., Genzel R., 2009, ApJL, 707, 114
Gillessen S., Eisenhauer F., Fritz T. K., Pfuhl O., Ott T., Genzel R., 2013, Proc. IAU Symp., Vol. 289, Advancing the Physics of Cosmic Distances. Cambridge Univ. Press, Cambridge, p. 29
Greiner J. et al., 2008, PASP, 120, 405
Haberl F., Eger P., Pietsch W., 2008, A&A, 489, 327
Hopman C., 2009, ApJ, 700, 1933
Israel G. L., Stella L., 1996, ApJ, 468, 369
Jansen F. et al., 2001, A&A, 365, L1
Juett A. M., Schulz N. S., Chakrabarty D., Gorczyca T. W., 2006, ApJ, 648, 1066
Kaspi V. M. et al., 2014, ApJ, 786, 84
Krühler T. et al., 2008, ApJ, 685, 376
Kuulkers E., den Hartog P. R., in't Zand J. J. M., Verbunt F. W. M., Harris W. E., Cocchi M., 2003, A&A, 399, 663
Lebrun F. et al., 2003, A&A, 411, L141
Lee H. M., 1995, MNRAS, 272, 605
Lund N. et al., 2003, A&A, 411, L231
Maan Y., Surnis M., Krishnakumar M. A., Joshi B. C., Manoharan P. K., 2016, The Astron. Telegram, 8729.
Maeda Y. et al., 2002, ApJ, 570, 671
Masetti N., Saito R. K., Rojas A. F., Minniti D., 2016, The Astron. Telegram, 8737
Miller J. M., Fabian A. C., Kaastra J., Kallman T., King A. L., Proga D., Raymond J., Reynolds C. S., 2015, ApJ, 814, 87
Miralda-Escudé J., Gould A., 2000, ApJ, 545, 847
Mori K. et al., 2013, ApJ, 770, L23
Morris M., 1993, ApJ, 408, 496
Muno M. P., Pfahl E., Baganoff F. K., Brandt W. N., Ghez A., Lu J., Morris M. R., 2005, ApJ, 622, L113

Muñoz-Darias T., Motta S., Belloni T. M., 2011, MNRAS, 410, 679
Muñoz-Darias T., Fender R. P., Motta S. E., Belloni T. M., 2014, MNRAS, 443, 3270
Nandra K., George I. M., Mushotzky R. F., Turner T. J., Yaqoob T., 1997, ApJ, 476, 70
Narayan R., Garcia M. R., McClintock J. E., 1997, ApJ, 478, L79
Neilsen J., Lee J. C., 2009, Nature, 458, 481
Nowak M. A. et al., 2012, ApJ, 759, 95
Pedicelli S. et al., 2009, A&A, 504, 81
Pfahl E., Loeb A., 2004, ApJ, 615, 253
Pinto C., Kaastra J. S., Costantini E., Verbunt F., 2010, A&A, 521, A79
Plotkin R. M., Markoff S., Kelly B. C., Körding E., Anderson S. F., 2012, MNRAS, 419, 267
Pons J. A., Rea N., 2012, ApJ, 750, L6
Ponti G., Cappi M., Dadina M., Malaguti G., 2004, A&A, 417, 451
Ponti G., Terrier R., Goldwurm A., Belanger G., Trap G., 2010, ApJ, 714, 732
Ponti G., Fender R. P., Begelman M. C., Dunn R. J. H., Neilsen J., Coriat M., 2012, MNRAS, 422, 11
Ponti G., Morris M. R., Terrier R., Goldwurm A., 2013, Astrophys. Space Sci. Proc., Vol. 34, Cosmic Rays in Star-Forming Environments. Springer-Verlag, Berlin, p. 331
Ponti G. et al., 2014a, in Sjouwerman L., Lang C., Ott J., Proc. IAU Symp., Vol. 303, The Galactic Center: Feeding and Feedback in a Normal Galactic Nucleus. Cambridge Univ. Press, p. 333
Ponti G., Muñoz-Darias T., Fender R. P., 2014b, MNRAS, 444, 1829
Ponti G., Bianchi S., Munoz-Darias T., De K., Fender R. P., Merloni A, 2015a, Astron. Nachr., 337, 512
Ponti G. et al., 2015b, MNRAS, 446, 1536
Ponti G. et al., 2015c, MNRAS, 453, 172
Ponti G. et al., 2015d, MNRAS, 454, 1525
Ponti G., Bianchi S., Muñoz-Darias-Darias T., De K., Fender R., Merloni A., 2016, Astron. Nachr., 337, 512
Predehl P., Schmitt J. H. M. M., 1995, A&A, 293,
Rea N., Esposito P., 2011, Astrophys. Space Sci. Proc., Vol. 21, High-Energy Emission from Pulsars and their Systems. Springer-Verlag, Berlin, p. 247
Rea N., Jonker P. G., Nelemans G., Pons J. A., Kasliwal M. M., Kulkarni S. R., Wijnands R., 2011, ApJ, 729, L21
Rea N. et al., 2013, ApJ, 775, L34
Remillard R. A., McClintock J. E., 2006, ARA&A, 44, 49
Revnivtsev M. G. et al., 2004, A&A, 425, L49
Reynolds M., Kennea J., Degenaar N., Wijnands R., Miller J., 2016, The Astron. Telegram, 8649
Smith R. K., Valencic L. A., Corrales L., 2016, ApJ, 818, 143
Strüder L. et al., 2001, A&A, 365, L18
Terrier R. et al., 2010, ApJ, 719, 143
Turner M. J. L. et al., 2001, A&A, 365, L27
Turolla R., Zane S., Watts A. L., 2015, Rep. Prog. Phys., 78, 116901
Ubertini P. et al., 2003, A&A, 411, L131
van der Klis M., 1988, in Ogelman H., van den Heuvel E. P. J., eds, NATO ASI Ser. C, Vol. 262, Timing Neutron Stars., Kluwer, Dordrecht, p. 27
Vaughan B. A. et al., 1994, ApJ, 435, 362
Vaughan S., Edelson R., Warwick R. S., Uttley P., 2003, MNRAS, 345, 1271
Verner D. A., Ferland G. J., Korista K. T., Yakovlev D. G., 1996, ApJ, 465, 487
Wallace L., Hinkle K., 1997, ApJS, 111, 445
Walter R., Lutovinov A. A., Bozzo E., Tsygankov S. S., 2015, A&AR, 23, 2
Wharton R. S., Chatterjee S., Cordes J. M., Deneva J. S., Lazio T. J. W., 2012, ApJ, 753, 108
White N. E., Mason K. O., 1985, Space Sci. Rev., 40, 167
Wijnands R. et al., 2006, A&A, 449, 1117
Wilms J., Allen A., McCray R., 2000, ApJ, 542, 914
Zdziarski A. A., Johnson W. N., Magdziarz P., 1996, MNRAS, 283, 193
Zhang S. et al., 2015, ApJ, 815, 132
Życki P. T., Done C., Smith D. A., 1999, MNRAS, 309, 561

This paper has been typeset from a TEX/LATEX file prepared by the author.